Available online at www.sciencedirect.com

ScienceDirect

Advances in Space Research 73 (2024) 5696–5713

ADVANCES IN SPACE RESEARCH (a COSPAR publication)

www.elsevier.com/locate/asr

Data Relay Constellation for high-performance links supply to future Martian missions

Daniele Barberi Spirito *, Jacopo Prinetto, Andrea Capannolo, Michèle Lavagna

Politecnico di Milano - Aerospace Science and Technology Department, Via G. La Masa, 34, Milano 20156, Italy

Received 21 November 2022; received in revised form 23 February 2024; accepted 26 February 2024
Available online 1 March 2024

Abstract

Over the last decade, the scientific interest in Mars drastically increased. The planned growth of the number of robotic missions, together with the sensors' increasing data acquisition capabilities and the expected crewed expeditions, entails a significant increase in data flow between the Martian assets and Earth both in volume and frequency of contact. In particular, crewed missions would lead to the need for nearly continuous communication with Martian assets. The keystone to avoid the future Martian telecommunication deadlock resides in specialising assets on specific functionalities through infrastructures. In this regard, the paper proposes a distributed Mars-based orbiting system servicing as a communication relay for any scientific and technological mission operating on the red planet's surface. The paper explores the design of a small satellites Martian constellation to maximise the surface coverage and visibility time with respect to ground users while reducing the station keeping efforts of the assets. A relatively novel proposed approach is to exploit the so-called Trans Areostationary Orbits (TASO), which allow low drift of the spacecraft with respect to Mars' surface, with an improved orbital stability than the perfectly stationary orbits. The paper aims at extending the available options by exploring trajectories that leverage the third body gravitation from the two Martian moons, Phobos and Deimos, to possibly further improve stability, coverage of the surface, communication datarates, and manoeuvres costs in general. The costs include the operative phase, as well as all the transfers from Earth to the Martian sphere of influence.As a final contribution, the paper explores the concept of Linked, Autonomous, Interplanetary Satellite Orbit Navigation (LiAISON) (Hill, 2007) for the proposed constellation configurations, to verify the possibility of reconstructing the spacecraft states through relative-only measurements.

Keywords: non-Keplerian dynamics; Martian constellation; Telecommunication; Mars Exploration; Mars

1. Introduction

The number of robotic missions headed to Mars has drastically increased over the last decade, and crewed expeditions are planned for future space programs. As far as the interest in Martian scientific missions increases, the amount of data collected is expected to overcome the state-of-the-art capabilities of the direct Earth-Mars link. Nowadays, scientific orbiters in polar low-altitude trajectories (Edwards et al., 2014; Bell et al., 2014) can support local missions with relay services. These satellites can guarantee full coverage of the Martian surface, but with short visibility windows followed by long communication gaps for near-equatorial users.

To cope with this problem, a local distributed infrastructure can be exploited to guarantee almost continuous communication for users in the near-equatorial region. Previous studies have been performed exploiting areostationary orbits (ASO) (Castellini et al., 2010) to increase the satellites' coverage and guarantee zero relative drift with respect to the surface. However, the irregular gravity field

* Corresponding author.
E-mail address: daniele.barberi@polimi.it (D. Barberi Spirito).

https://doi.org/10.1016/j.asr.2024.02.053
0273-1177/

of Mars generate instability regions on the orbit (Montabone et al., 2020), causing the spacecraft of a constellation on such orbit to drift apart. An alternative to ASO is represented by the so-called Trans Areostationary Orbits (TASO), characterized by a slightly higher altitude (about 600 km above). This causes a secular drift of the spacecraft with respect to the Martian surface; nevertheless, the irregularities of the planet's gravity field couple interact with spacecraft motion on such orbit, cancelling out the average relative drift between them (Parfitt et al., 2021). The downside of this strategy is a slightly lower datavolume that can be managed by the constellation, due to the longer distance from the surface, and the requirement of a very good initialization to actually nullify the relative drift. The present work wants to explore alternative configurations based on trajectories in the multi-gravity regimes of Mars and its moons, Phobos and Deimos. Advantages in leveraging the gravity of the moons are studied in terms of orbital maintenance and stability, station-keeping costs, as well as coverage and datarate-datavolume manageable by the constellation. The proposed new strategies are also compared with respect to the TASO scenario. Finally, the paper analyses a relatively recent navigation strategy called "Linked, Autonomous, Interplanetary Satellite Orbit Navigation" (LiAISON), based on relative-only measurements, for the proposed multi-gravity constellation configurations (Hill, 2007; Barberi Spirito, 2021). Indeed, the asymmetry of the field experienced in multi-gravity regimes makes the full constellation's state observable through relative range and range-measures only, and potentially increases the autonomy of the systems by lifting the navigation burden from Earth's ground segment. The paper is structured as follows.

In Section 2 the mathematical background is given both for the gravitational models exploited and the transfer optimisation tool. In Section 3 the considered of merit are presented together with the trajectories analysed for the constellation design. Performances of the different architectures are then reported. In Section 4 the performance of the proposed constellations are analysed, based on the previous figures of merit. In Section 5 the possibility of autonomous self-calibration with relative measurements only is assessed, while in Section 6 conclusive remarks are reported.

2. Background

2.1. Dynamics model

The preliminary design and analysis of the proposed orbital solutions are carried out through two dynamical models, namely the *Restricted Two-Body Problem* (R2BP) and the *Circular Restricted Three-Body Problem* (CR3BP). A third, high-fidelity dynamics model is then employed to verify the boundedness of the proposed orbits. The three models are hereafter described.

R2BP. The formulation of the R2BP foresees a single massive attractor, with the orbiting object not generating any gravitational field. The equations of dynamics read

$$\ddot{\mathbf{r}} = \nabla U \tag{1}$$

where the $\ddot{()}$ superscript denotes the second derivative in time, and U is the gravitational potential, described in the next section.

CR3BP. The CR3BP foresees two massive attractors describing circular orbits around their centre of mass. The third body (in this case, the spacecraft) is assumed to have a considerably lower mass not to interfere with the natural motion of the massive bodies. With these assumptions, the equations of motion (properly made non-dimensional according to the attractors' mass, distance and characteristic time) read:

$$\begin{aligned} \ddot{x} - 2\dot{y} &= \frac{\partial \mathscr{U}}{\partial x} \\ \ddot{y} + 2\dot{x} &= \frac{\partial \mathscr{U}}{\partial y} \\ \ddot{z} &= \frac{\partial \mathscr{U}}{\partial z} \end{aligned} \tag{2}$$

where the right-hand side terms are the spatial derivatives of a pseudo-potential function $\mathscr{U}$, defined as:

$$\mathscr{U} = \frac{1}{2}\left(x^2 + y^2\right) + \widetilde{U}_1 + \widetilde{U}_2 \tag{3}$$

with $\widetilde{U}_1$ and $\widetilde{U}_2$ being the potential of the two attractors of the binary system, in the non-dimensional form.

High-fidelity model. The employed high-fidelity model leverages the data from ephemerides of all the main attractors of the Solar System, as well as Phobos and Deimos. The gravity models for the attractors (explained in detail in the next section) are "spherical harmonics" (SH) up to the 20th degree for Mars, "ellipsoid" (Ell) for Phobos and Deimos, and "point mass" (PM) for all the other planets and the Sun. The reference frame is inertial, centred in the Mars system barycentre, and aligned with "Mars Mean Equator and IAU vector of J2000". The acceleration vector reads:

$$\begin{aligned} \ddot{\mathbf{r}} = {} & \nabla \mathbf{U}^{(\mathbf{SH})}_{\mathbf{Mars}} + \nabla \mathbf{U}^{(\mathbf{Ell})}_{\mathbf{Phobos}} + \nabla \mathbf{U}^{(\mathbf{Ell})}_{\mathbf{Deimos}} \\ & + \sum_{\substack{\mathbf{j} \in \mathbf{Planets,Sun} \\ \mathbf{j} \neq \mathbf{Mars}}} \left(\nabla \mathbf{U}^{\mathbf{PM}}_{\mathbf{j}} - \nabla \mathbf{U}^{\mathbf{PM}}_{\mathbf{j} \rightarrow \mathbf{Barycentre}} \right) \end{aligned} \tag{4}$$

where the last subtracted term is the gravity effect of the other celestial bodies on Mars system's barycentre moving around the Sun.

2.2. Gravitational models

Point mass gravity. When the dynamics is described through point mass attractors, the potential reads:

$$U = \frac{Gm}{r} \tag{5}$$

with G being the gravitational constant, m is the attractor's mass, and r is the second mass' distance from the main

attractor. In the case of the non-dimensional expression for the CR3BP (used in Eq. 3), Eq. 5 takes the following forms for the first and second attractor respectively

$$\widetilde{U}_1 = \frac{1-\mu}{r_1} \tag{6}$$

$$\widetilde{U}_2 = \frac{\mu}{r_2} \tag{7}$$

where r_1 and r_2 are the relative distances of the third body from the two attractors, and μ is the system mass fraction, defined as:

$$\mu = \frac{m_2}{m_1 + m_2} \tag{8}$$

Ellipsoid gravity. In the case of an ellipsoidal attractor (this model will be used for the gravity generated by the moons of Mars), the formula derived by MacMillan (Andrews, 1930) can be used, i.e.:

$$U = \frac{2G\rho\pi abc}{\sqrt{a^2-c^2}}\left\{\left[1-\frac{x^2}{a^2-b^2}+\frac{y^2}{a^2-b^2}\right]F(\omega_\kappa,k) + \left[\frac{x^2}{a^2-b^2}-\frac{(a^2-c^2)y^2}{(a^2-b^2)(b^2-c^2)}+\frac{z^2}{b^2-c^2}\right]E(\omega_\kappa,k) + \left[\frac{(c^2+\kappa)y^2}{b^2-c^2}-\frac{(b^2+\kappa)z^2}{b^2-c^2}\right]\frac{\sqrt{a^2-c^2}}{\sqrt{(a^2+\kappa)(b^2+\kappa)(c^2+\kappa)}}\right\} \tag{9}$$

Here, a, b, c are the three semi-axes of the ellipsoid in decreasing length order, ρ is the mean density of the body, F, E are the Legendre's elliptic integrals of first and second kind respectively, and ω_κ and k satisfy the conditions in Eq. 10 and 11.

$$\sin(\omega_\kappa) = \sqrt{\frac{a^2-c^2}{a^2+\kappa}} \tag{10}$$

$$k^2 = \frac{a^2-b^2}{a^2-c^2} \tag{11}$$

Spherical harmonics. Given the importance (for the cases under study) of the spherical harmonics generated by Mars' shape, the gravitational potential is expressed through Eq. 12.

$$U = \frac{Gm}{r}\left\{1+\sum_{i=2}^{n}\sum_{j=0}^{i}\left(\frac{R_0}{r}\right)^i\left[C_{ij}\cos(j\lambda)+S_{ij}\sin(j\lambda)\right]P_{ij}(\cos(\theta))\right\} \tag{12}$$

λ and θ are the attractor's longitude and co-latitude respectively, R_0 a reference radius (typically the average equatorial radius), $P_{ij}(x)$ are *Associated Legendre Polynomials* (Belousov, 2014), while C_{ij} and S_{ij} are the normalised Stokes coefficients, computed as:

$$\begin{aligned} C_{ij} &= \frac{1}{m}\sqrt{\frac{(2-\delta_{0j})(i-j)!}{(2i+1)(i+j)!}}\iiint_m\left(\frac{r}{R_0}\right)^i P_{ij}(\sin(\theta))\cos(j\lambda)dm \\ S_{ij} &= \frac{1}{m}\sqrt{\frac{2(i-j)!}{(2i+1)(i+j)!}}\iiint_m\left(\frac{r}{R_0}\right)^i P_{ij}(\sin(\theta))\sin(j\lambda)dm \end{aligned} \tag{13}$$

2.3. The Martian moons

Given the fundamental role of Phobos and Deimos in the design of the proposed constellation architectures, it is important to specify the main characteristics of these celestial objects. Phobos is the closest moon to the Martian surface, orbiting at approximately 6000 km of altitude, far below the areostationary orbital region, and with a nearly circular motion around the Red Planet. Also, its orbit is almost planar with respect to Mars' equator. This makes the moon pass above the equatorial region around twice a Martian day. Its shape can be approximates as the one of an ellipsoid having the three axes of length 27 km, 22 km and 18 km, and tidally locked to mars along its largest axis. Deimos' average altitude is close to 20100 km, around 3000 km above the areostationary orbit, with an eccentricity and an inclination lower than Phobos', which translates to a slow retrograde motion with respect to the Martian surface. As for Phobos, Deimos can be approximated as an ellipsoid with axes 15 km, 12 km, and 11 km long. Like Phobos, Deimos is also tidally locked with respect to Mars. The whole set of Phobos and Deimos orbital parameters is reported in Table 1.

2.4. Optimisation tool

The design of an efficient constellation deployment demands a proper selection of optimisation techniques. To maintain a certain level of realism for the analysis, limited on-board resources have been taken into account. In particular, a maximum available thrust-to-weight ratio is considered for the mission. This suggests the exploitation of two sequential optimisation steps, hereafter described.

Impulsive trajectory design. The design of the impulsive trajectories was conducted using a simple but effective two-body problem with the assumption of patched conics. Indeed, in this case, it is possible to find closed analytical solutions that turn the continuous control problem into a parametric optimisation one (Battin, 1999). To rapidly and effectively find a near-optimal solution to the resulting parametric problem, Heuristics algorithms were preferred (Pearl, 1984), and in particular, a Particle Swarm optimisation algorithm was implemented (Poli, 2008) (Kennedy and Eberhart, 1995).

Finite thrust optimisation. For finite burn manoeuvres (realistic manoeuvres modelled upon a maximum thrust value and thrust time) Direct Transcription and Collocation algorithm is used. These optimised manoeuvres are

Table 1
Martian moons' main orbital parameters in Martian equatorial reference frame.

	Semi-major axis [km]	Eccentricity [-]	Inclination [deg]	Orb. Period [hr]
Phobos	9376	0.0151	1.093	7.65
Deimos	23463	0.0003	0.930	30.31

then used to estimate the Gravity Losses (GL), i.e performance reductions caused by the non-impulsive nature of the finite burn. To quantify the effect of the GL on the overall ΔV, some relevant trajectories, such as the Mars Insertion Manoeuvre and the pericentric Earth Escape manoeuvre, were designed considering a finite $\frac{T}{m}$ ratio. In particular, to optimise the trajectories, a *Hermite-Simpson* Direct Transcription and collocation algorithm was adopted (Topputo and Zhang, 2014) (Conway and Paris, 2010) (Prinetto and Lavagna, 2021).

3. Constellation design criteria

In this section, the candidate trajectories for the constellation design are presented together with the figures of merit that guided the definition of the architectures. Then, the possible alternatives are analysed and the performances in terms of ΔV budgets and data transmission are presented.

3.1. Figures of merit

The figures of merit that drove the selection of the architecture are reported and explained in this section. The parameters are selected to take into account both the performances of the constellation, in terms of service provided to the user (i.e. telecommunication coverage and data transmission), and the costs of insertion and maintenance of the desired trajectories. Hence, the parameters evaluated during the study are:

- *Station keeping budget:* intended as the ΔV budget required to maintain the operative trajectories for a mission operative lifetime of 6 years. It sizes the propellant mass of the satellites and shall be minimised.
- *Transfer budget:* the ΔV budget required to achieve the target orbit starting from an Earth-bounded trajectory dependent on the selected scenario, as further explained in Section 4.2.
- *Temporal Coverage:* the visibility time per day between a user on the Martian surface in the near-equatorial region and one of the constellation satellites.
- *Data-rate:* influences the velocity of the connection. Hence, a higher data-rate can guarantee the transmission of the desired amount of data with a lower visibility time.
- *Data-volume:* the amount of data transmitted from the user to the constellation satellites is an output of the achieved coverage and data-rate. This parameter is crucial for the architecture definition since it influences the total amount of information that can be extracted from surface users in the given amount of time.

3.2. Orbit types

The candidate architectures are defined as a combination of significant trajectories with periodic visibility properties with respect to the Martian surface, presented in the following paragraphs.

Trans-Areostationary Orbits (TASO). The nominal TASO is a circular orbit, having a semi-major axis of 21000 km, slightly above the areostationary orbits (Spirito et al., 2021; Montabone et al., 2020). Such trajectory, although not stationary with respect to Mars's surface (15° drift per Martian sidereal day), ensures a higher stability degree than the synchronous orbit. The relative drift between satellites placed nearby such orbit can be minimised by proper tuning of the initial altitude of each element of the constellation, leveraging the spherical harmonics of Mars' gravity. Such initial altitude is strongly dependent on the initial Mars's surface orientation and, therefore, needs to be correctly computed once the initial date of the operational life of the satellite is set. Fig. 1 (part a) shwos the relative trajectory of one spacecraf with respect to the other in the high-fidelity model, when the constellation is properly initialised. Fig. 1 (part b) shows instead the time variation of the phase difference. It is observed that, despite minor oscillations of the "phase difference" (the angle between the two spacecraft, with Mars being the vertex), the oscillations are bounded throughout the whole mission span of 6 years. It is, however, worth noting that such optimal condition is very sensitive to the initialisation of the constellation. For example, an error on the initial altitude of one spacecraft about 100 m is sufficient to make it drift apart (if no active control is applied).

Quasi Satellite Orbits (QSO). QSO are trajectories hovering around the moon of the binary system (Mars-Phobos or Mars-Deimos) and are subjected to the attraction of the two bodies almost equally. The result is a formation-flying-like trajectory around the moon, which however is stabilised by the latter, removing the relative drift that typically arises from formations of non-attracting objects (such as two artificial satellites). Fig. 2 depicts an example of a QSO in the Mars-Phobos binary system. The stability of the QSO is verified within some ranges also in the high-fidelity dynamical model. In particular, stable QSO around Phobos were found at distances from the moon between $50 - 100$ km, while distance values between $16 - 56$ km were identified for QSO around Deimos. Fig. 3 depicts the long term stability of a sample QSO in the Phobos environment.

Horseshoe Orbits (HS). HS are Keplerian-like orbits with altitude and period similar to those of the moon of the system. A satellite placed in such orbit would have a very slow drift with respect to the moon (depending on the altitude differences between the two). When approaching the secondary body, a satellite in such orbit naturally executes a flyby of the moon, changing its semi-major axis and gaining distance from the moon itself, until the next encounter. Such low-paced drift may be exploited to minimise station-keeping costs for relative phase maintenance between satellites. Despite the nominal long-term drift, perturbations may accelerate such a process, therefore a proper optimisation would be needed to have the minimum

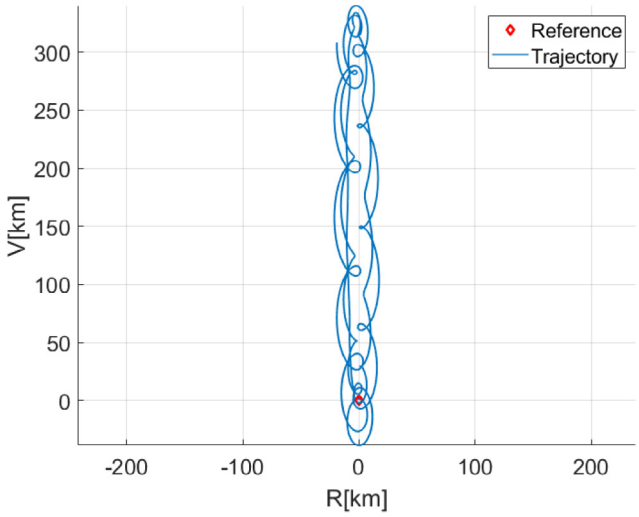

(a) Relative trajectory in the Local Vertical Local Horizontal frame. The red square represents the point at fixed phase difference from thesecond spacecraft. The trajectory is here depicted for 30 days only, for a better visibility of the relative motion.a

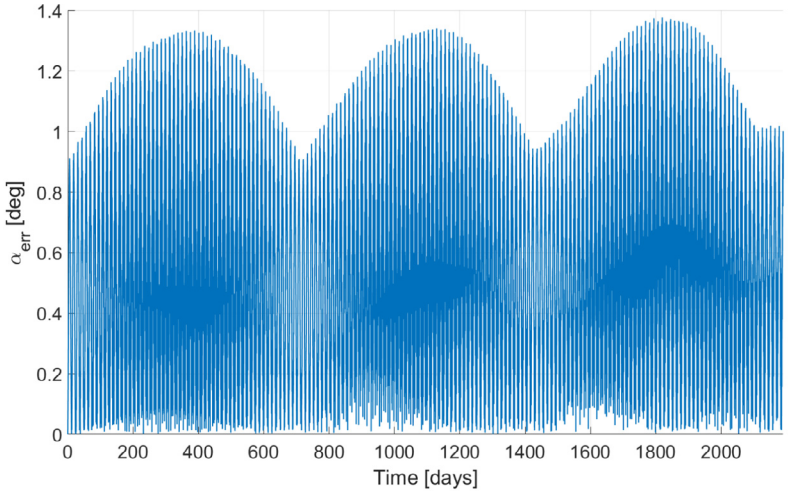

(b) Relative phase angle difference (absolute value) within a 6 years time span.

Fig. 1. Evolution of the relative motion for one spacecraft on the TASO with respect to a second one. Dynamics propagated in the high-fidelity model.

drift possible, as for the TASO scenario. Fig. 4 depicts an example of an HS in the Mars-Phobos binary system.

When propagated in the high-fidelity model, the HS orbits of the Mars-Phobos and Mars-Deimos binary systems maintain their stability, although the regular motion depicted in Fig. 4 becomes more complex. The result is a bounded motion in the annular region of the binary system, as depicted in Fig. 5 for a 6 years propagation in the Mars-Phobos environment. Fig. 6 depicts the detail of the motion in the annular region. It can be observed that the spacecraft describes a fairly even oscillatory motions in the Phobos orbital plane, which however couples with an out-of-plane oscillation that reduces the overall regularity of the trajectory. It is however worth noting that while the in-plane oscillations cover hundreds of kilometres, the out-of-plane motion will have an amplitude slightly above one kilometre.

4. Constellation performances analysis

In this section, the possible configurations are presented in terms of combination of trajectories presented in Section 3. Then, the figures of merit are computed for each configuration and a summary of the configuration performances is presented.

4.1. Constellation configurations and performance

Given the orbit types explored in Section 3.2, 3-satellite constellations are explored in the specific environments of Phobos, Deimos and in the TASO region, namely:

- Equally spaced (120°) spacecraft along the TASO.
- 1 QSO satellite around Phobos, and 2 HS satellites equally shifted from Phobos at ±120°.

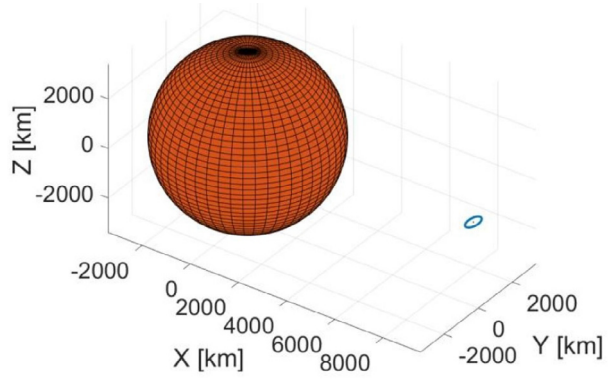

(a) Full binary system.

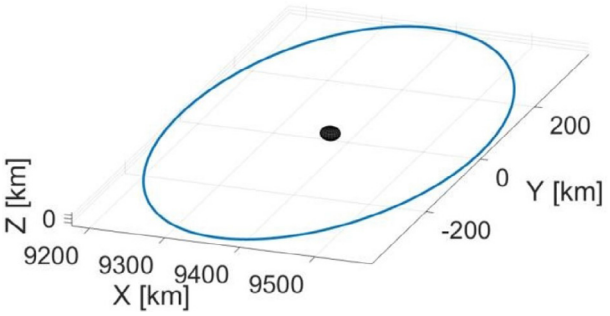

(b) Zoom nearby the moon.

Fig. 2. Example of a QSO in the Mars-Phobos system with CR3BP dynamical model.

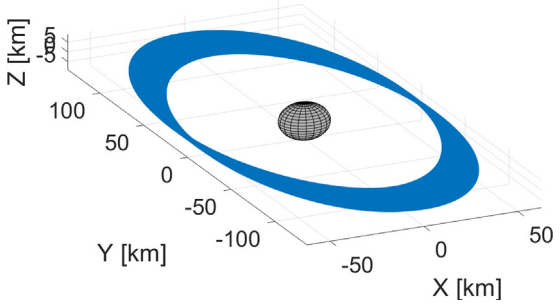

Fig. 3. QSO in the high-fidelity environment for a 6 years time span.

- 1 QSO satellite around Deimos, and 2 HS satellites equally shifted from Deimos at ±120°.

These combinations are hereafter evaluated in terms of cost (transfers, station-keeping, relative phasing) and communication/coverage performance.

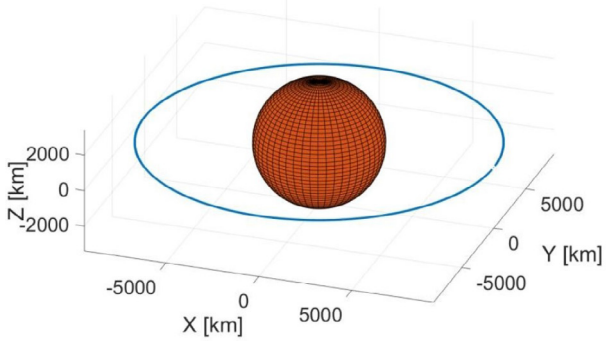

(a) Full binary system

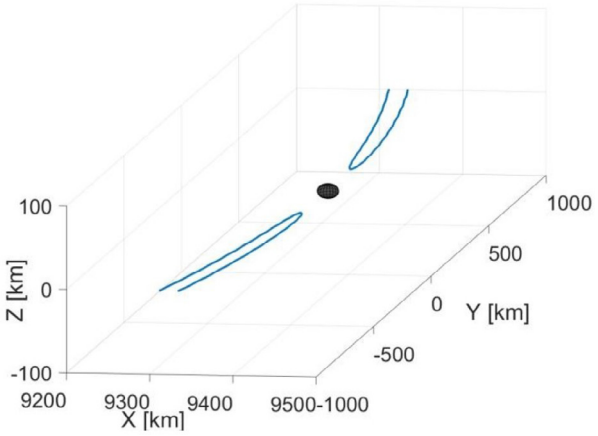

(b) Zoom nearby the moon

Fig. 4. Example of a HS in the Mars-Phobos system.

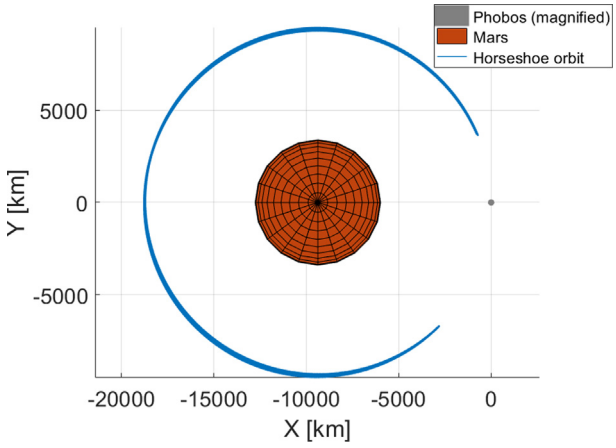

Fig. 5. High-fidelity propagation of a HS orbit in the Mars-Phobos binary system, for a time space of 6 years. Trajectory represented in the Mars-Phobos rotating frame.

4.2. Transfer Strategies

For the trajectory design and optimisation, the patched conics method was applied. Therefore the trajectory itself is divided into three different phases:

1. *Earth Escape:* in this phase the spacecraft shall escape from the Earth's gravity field, matching the boundary conditions (mainly C3 and asymptote declination) required by the interplanetary trajectory. Different strategies will be considered.

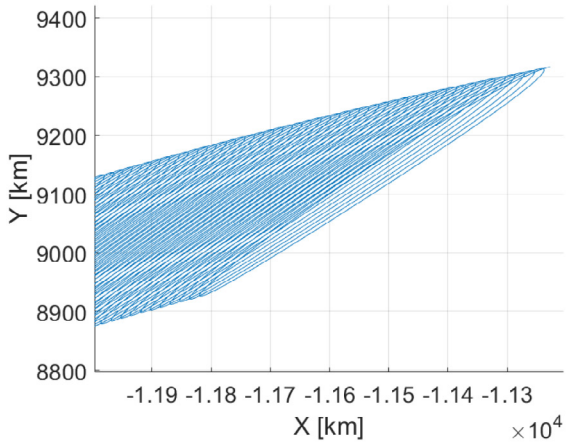

(a) X-Y plane projection.

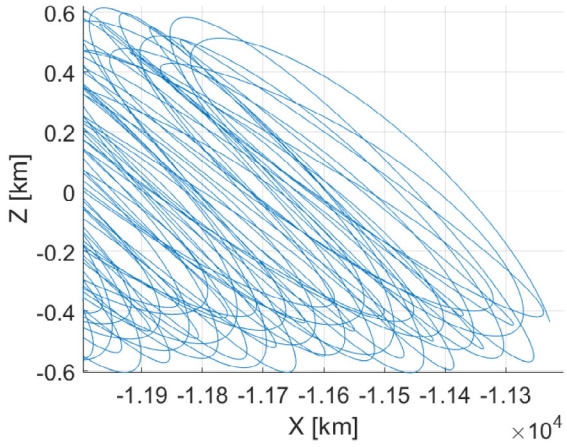

(b) X-Z plane projection.

Fig. 6. Detail of the high-fidelity spacecraft motion on the Mars-Phobos HS orbit. Trajectory propagated for one year only, and zoomed on its final part for better visualisation of the motion.

2. *Interplanetary Trajectory:* in this phase the spacecraft travels from the Earth's sphere of influence to Mars' one.
3. *Mars Capture:* in this case the spacecraft shall close the trajectory around Mars and reach the correct operational orbit, matching the boundary conditions (mainly C3 and asymptote declination) required by the income interplanetary trajectory.

In the following paragraphs all the phases are detailed, as well as the relevant methodologies adopted.

4.2.1. Interplanetary trajectory

The interplanetary trajectory between Earth and Mars consists of one Lambert's arc linking the two bodies, implying only natural motion in this phase. The position of the solar system bodies is computed using analytical ephemerides, valid between 1800 AD and 2050 AD. Fig. 7 and Fig. 8 show the asymptotic velocity and the declination of the asymptote for the launch window occurring during 2026. More in detail, the reported solutions are the ones with an escape C3 limited to $10\frac{km^2}{s^2}$ and declination at the departure limited to 30°. The resulting launch window ranges from October 19^{th} to November 9^{th}; a wider launch window is possible if a higher C3 is considered. Fig. 9 shows the fuel-optimal interplanetary trajectory.

4.2.2. Earth escape

The Earth escape trajectory aims to inject the spacecraft into the correct hyperbolic trajectory. The main parameters that characterise the escape hyperbola are the Right Ascension (RA) and the declination of the asymptote, as well as the infinite velocity. In particular, the declination of the asymptote and the infinite velocity are fundamental to investigate the ΔV required and consequentially the propellant mass to be embarked, while the RA, together with the epoch, is useful to determine the Right Ascension of the Ascending Node (RAAN) of the parking orbit. To match the 21 days launch window requirement, a C3 of $10\frac{km^2}{s^2}$ and a declination of 30° were considered during the design of the escape trajectories. To have a wide overview of the different possible solutions, the following scenarios have been analysed:

- Direct Hyperbolic Escape
- High Elliptical Orbit (HEO) Departure
- Geostationary Transfer Orbit (GTO) Departure
- GTO Departure with perigee Local Time constraint
- GTO Departure with Moon-Earth Gravity Assist (GA)

The trajectories are computed considering impulsive manoeuvres only but, to take into account the GL, some specific trajectories were optimised considering finite thrust, through a Hermite-Simpson direct transcription algorithm. After that, three different scenarios arise:

1. *Apocentric Manoeuvres*: GL are negligible due to the low velocity of the spacecraft.
2. *Pericentric Manoeuvres with low* ΔV *(*$\Delta V < 100$ *m/s)*: GL are negligible due to the small duration of the manoeuvres.
3. *Pericentric Manoeuvres with high* ΔV *(*$\Delta V > 100$ *m/s)*: 15% of the impulsive values.

Direct Hyperbolic Escape. In this strategy, the upper stage of the launcher shall directly inject the spacecraft into the escape hyperbola. Table 2 shows the launchable masses for the mission-relevant European launchers at the desired C3 $= 10\frac{km^2}{s^2}$ and declination of 30° (conservative scenario).

The drawback of this strategy is that, in most cases, a dedicated launch is required, therefore the cost up to the launch is larger compared with the other strategies. Even if in the nominal scenario this strategy doesn't include manoeuvres up to the spacecraft, a $30m/s$ margin is applied, following the ECSS Margin Philosophy for Mars Exploration Studies (HRE-XE-ESA, 2017).

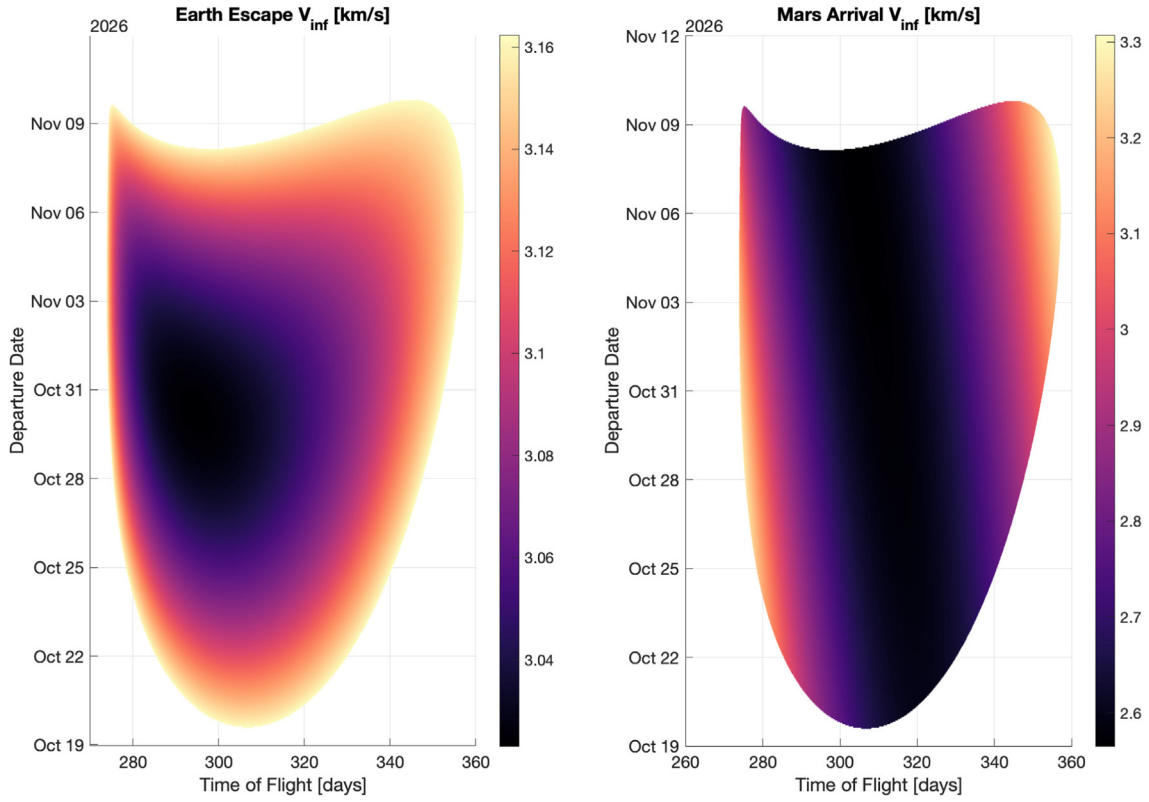

Fig. 7. Departure and arrival asymptotic velocities.

HEO Departure. In this strategy, the launcher injects the spacecraft in a HEO with Keplerian parameters as in Table 3, as from Ariane 6 User Manual (Arianespace, 2021). The energy of the resulting orbit is high, and therefore the cost of the pericentric manoeuvre to reach the desired hyperbola is extremely reduced if compared to lower departure orbits, such as GTOs. Moreover, if the node of the HEO is correctly aligned with the RA of the asymptote, the change of plane is also reduced. Table 4 shows the ΔV breakdown. The strategy depicted in Fig. 10 includes three burns to reach the correct asymptote.

GTO Departure – Unconstrained Pericenter Local Time. In this strategy, the spacecraft is injected by the launcher in a dedicated GTO, whose parameters are taken from Ariane 6 User Manual (Arianespace, 2021) and listed in Table 5. A scheme of the strategy trajectories is depicted in Fig. 11. The strategy to escape from this orbit includes three different burns with an intermediate highly eccentric orbit. The higher the semi-major axis of the intermediate orbits, the lower the departure cost. Anyway, the perturbations for extremely high elliptic orbits could be not negligible and some correction manoeuvres shall be necessary. In the presented solution, an apocenter of approximately 900000 km is considered for the change of plane manoeuvre. The worst-case breakdown of the ΔV necessary to escape from GTO following this strategy is presented in Table 6.

GTO Departure – Constrained Pericenter Local Time (midnight). To increase the flexibility of the mission scenario in case of a ride-share launch, a further constraint on the Local Time of the pericenter is included. More precisely, the sun angle of the eccentricity vector is forced to be 12 h (i.e., the Local Time of the pericenter is midnight). In this scenario, the exact value of the ΔV strongly depends on the departure date and the interplanetary Time Of Flight (TOF). Indeed, the local time of the asymptote is not constant during the 3 weeks launch window. Fig. 12 shows the ΔV required as a function of the departure date and the interplanetary TOF. To guarantee the above-mentioned launch window of three weeks, it is necessary to size the system for a ΔV of $1,71\frac{km}{s}$. Table 7 shows the ΔV breakdown for the worst-case solution that can satisfy the 3 weeks launch window requirement.

GTO Departure - Moon-Earth GA. In this strategy, the spacecraft is injected by the launcher into a GTO. To reduce the escape cost, the trajectory takes advantage of a Moon-Earth GA, ad in (Penzo, 1998). The resulting ΔV required for the GTO escape including a GA around the Moon is between 1.2 km/s and 1.4 km/s, depending on the RA of the Moon and the one of the asymptote. Fig. 13 shows the departure trajectory for this strategy. To perform a safe GA the minimum altitude of the periapsis of the hyperbola above the Moon is set equal to 100 km. Table 8 shows the ΔV breakdown for a conservative solution. On the other hand, it is important to underline that this strategy imposes tight constraints on the operations due to the necessity to have a correct alignment of the

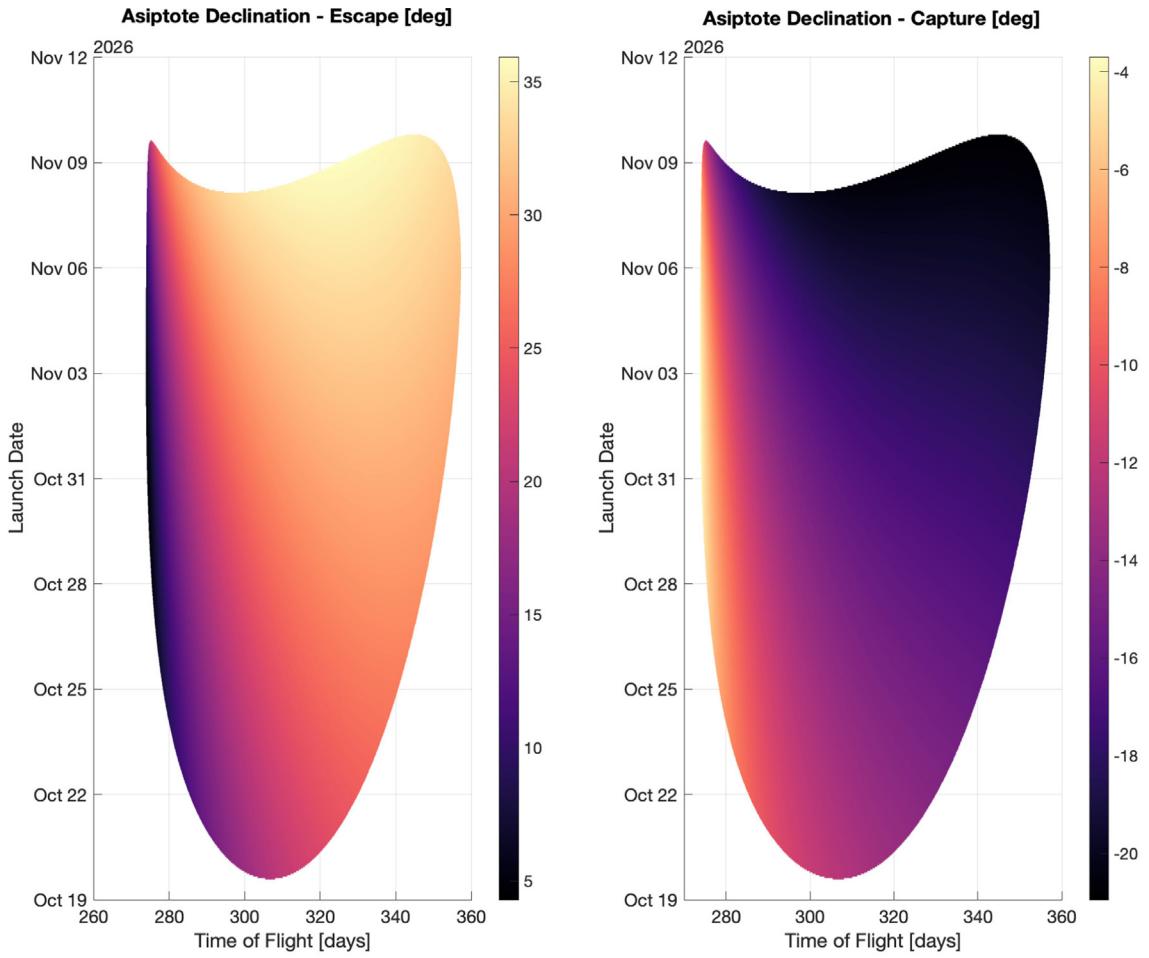

Fig. 8. Departure and arrival asymptote declination.

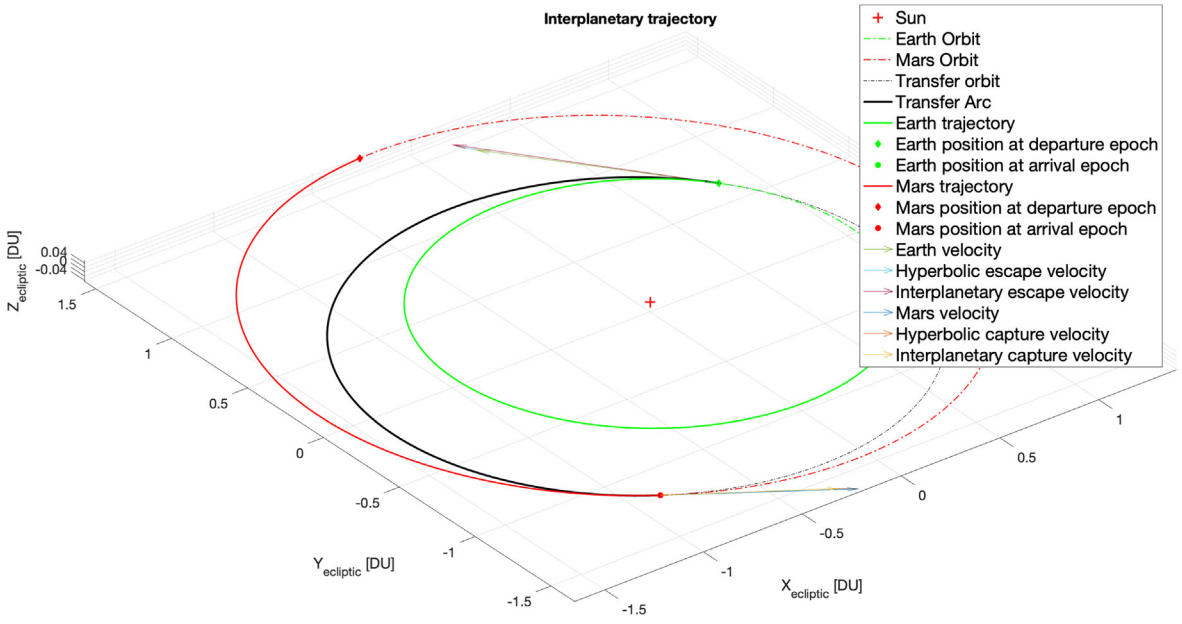

Fig. 9. Fuel optimal interplanetary trajectory for 2026 launch window.

Table 2
European launcher comparison for direct injection.

Launchers	Launchable mass [kg]
Ariane 62	1800 kg
Ariane 64	5500 kg

Table 3
HEO Keplerian parameters.

Parameter	Value
Pericenter altitude	250 km
Apocenter altitude	900000 km
Inclination	6°
RAAN	Free (part of the opt.vector)
Pericenter arg.	178°
True anomaly	Free (part of the opt.vector)

Table 4
HEO Departure strategy ΔV breakdown for single manoeuvres (worst case considered).

Man.	ΔV [km/s]	Gravity Losses	Margin Policy	ΔV [km/s]
First	0.0086	0%	10 m/s	0.019
Second	0.111	0%	10 m/s	0.121
Third	0.530	15%	5%	0.641
TOT.	**0.650**			**0.781**

launcher and Moons planes that could lead to an unacceptable increase on the complexity of the mission itself.

4.2.3. Mars Capture

The ΔV required for the Mars capture manoeuvre depends on the target orbit. To include a sufficient wide launch window (21 days) a C3 of $9\frac{km^2}{s^2}$ and a declination of $-10°$ have been considered for the arrival hyperbola. Differently from the departure strategy, to reduce the cost of the Mars capture, a GA is not effective due to the low masses of the Martian moons. Moreover, due to the altitude of the operational orbits, aerobraking is not convenient. On the other hand, for all of the analysed strategies, it is possible to substitute the first pericentric manoeuvre with an aerocapture strategy (Isoletta et al., 2021), saving $940m/s$ ($1.087km/s$ if GL and margins are applied as in (HRE-XE-ESA, 2017)). For all the scenarios a 4Sol Mars Orbit Insertion (MOI) has been considered. The adopted propulsive system consists of a storable bi-propellant thruster with $800N$ of thrust and $320s$ of specific impulse. The mass injected in the 4Sol parking orbit is equal to $1000kg$. The ΔV increases from $940m/s$ to $989m/s$ due to GL, that are quantifiable as the $5,1\%$. To be conservative with respect to the dry mass changes, a 10% GL is considered in the following scenarios. The same effect of the GL is adopted for all the pericentric manoeuvres, while they are discarded for the apocentric ones, due to the slow dynamics involved.

Table 5
GTO Keplerian parameters.

Parameter	Value
Pericenter altitude	250 km
Apocenter altitude	35786 km
Inclination	6°
RAAN	Free (part of the opt.vector)
Pericenter arg.	178°
True anomaly	Free (part of the opt.vector)

TASO. The strategy includes three manoeuvres to get the correct shape and plane. The ΔV required depends on the apocentric altitude of the plane change orbit: the higher the apocenter, the lower the cost. The ΔV breakdown considering a 4Sol MOI is reported in Table 9. Fig. 14 shows the capture trajectory.

Phobos Environment. The strategy is depicted in Fig. 15, and includes three manoeuvres to get the correct shape and plane. As for the TASO, the ΔV required depends on the period of the plane change orbit: the higher the apocenter, the lower the cost. The ΔV breakdown considering a 4Sol MOI is reported in Table 10.

Deimos environment. The strategy is depicted in Fig. 16, in the same fashion of the Phobos transfer strategy. The ΔV breakdown, always taking as reference a 4Sol MOI, is reported in Table 11.

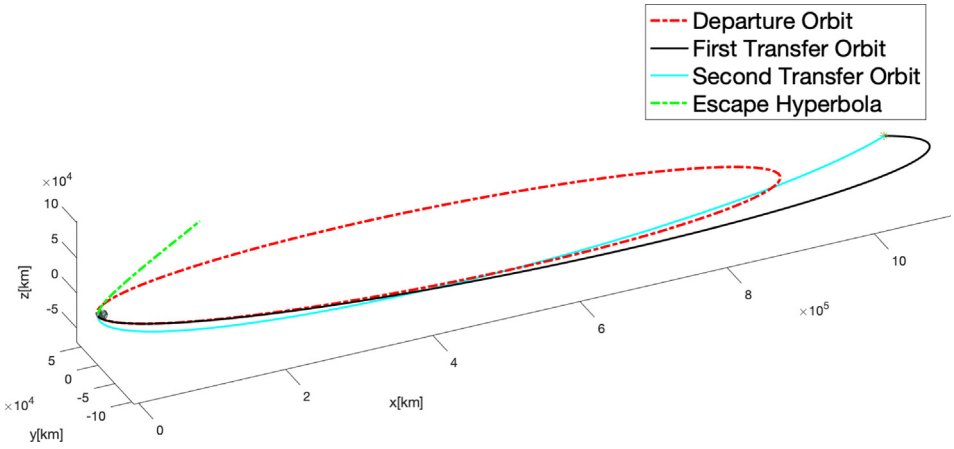

Fig. 10. Example of HEO departure trajectory.

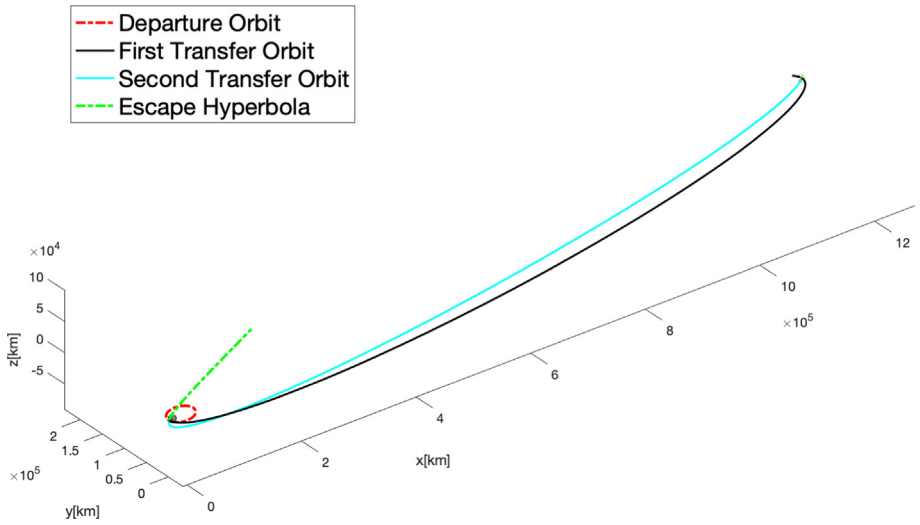

Fig. 11. Example of GTO departure trajectory.

Table 6
ΔV breakdown for GTO departure strategy - worst case.

Man.	DV [km/s]	Gravity Losses	Margin Policy	DV [km/s]
First	0.734	15%	5%	0.886
Second	0.094	0%	10 m/s	0.099
Third	0.485	15%	5%	0.607
TOT.	**1.313**			**1.592**

4.2.4. ΔV budgets summary

In Tables 12–14 the costs are summarised for TASO, Phobos and Deimos scenarios respectively. For the three scenarios, both the costs in terms of Departure and Capture, independent on the selected Earth escape strategy, are reported.

4.3. Phasing and station-keeping analysis

Once the insertion of the spacecraft into the final operative orbits is completed, two types of manoeuvres have to be considered:

- *Phasing* (manoeuvres to correctly distribute the formation around the planet).

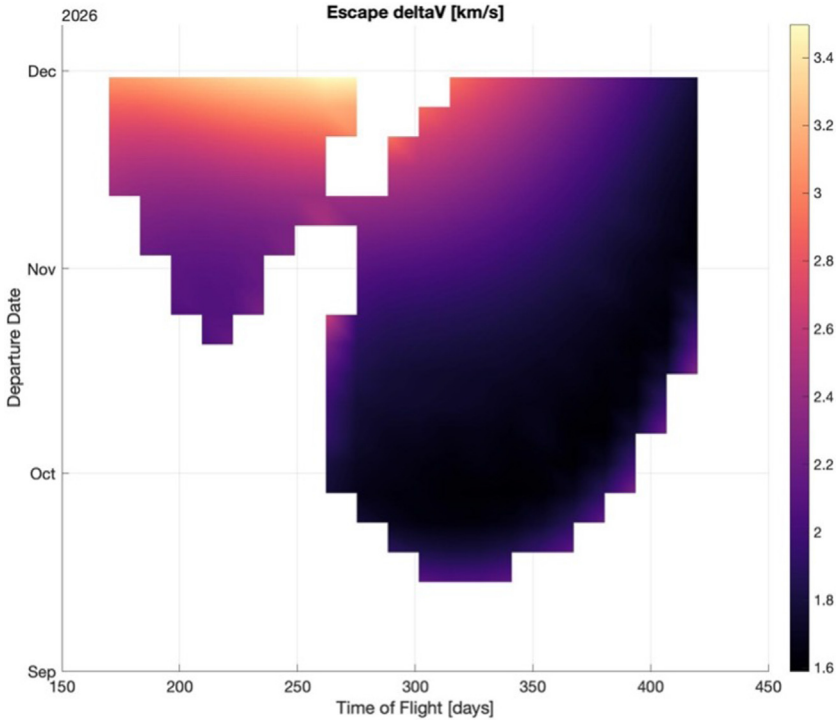

Fig. 12. GTO escape ΔV map - constrained Local Time of Pericenter.

Table 7
ΔV breakdown for GTO departure strategy - constrained Local Time of Pericenter.

Man.	DV [km/s]	Gravity Losses	Margin Policy	DV [km/s]
First	0.769	15%	5%	0.928
Second	0.015	0%	10 m/s	0.025
Third	0.928	15%	5%	1.121
TOT.	**1.71**			**2.074**

Table 8
ΔV breakdown for GTO + Moon GA departure strategy - constrained Local Time of Pericenter.

Man.	DV [km/s]	Gravity Losses	Margin Policy	DV [km/s]
First	0.787	15%	5%	0.950
Second	0.0	0%	10 m/s	0.01
Third	0.624	15%	5%	0.754
TOT.	**1.41**			**1.714**

- *Station-Keeping* (manoeuvres to correct perturbations' effects and keep all spacecraft around their nominal position).

Phasing. In this study, we assume that the three spacecraft of the formation are injected together in the final operative region. Also, we assume that the location when the injection happens is already the final operative point for one of the three spacecraft. This implies that only two elements of the formation will need to perform phasing manoeuvres, to reach their respective operative points. In the TASO constellation case, the spacecraft share the same orbit, so the choice of the satellite that will be correctly initialised from the beginning is irrelevant. Concerning the QSO + HS constellations, we assume that the spacecraft orbiting on the QSO will always be the one correctly located from the beginning of the operative phase, and that the other two satellites will need the phasing manoeuvre to move to their respective points on the HS. This is justified by a minimised propellant need from the QSO-orbiting spacecraft, and an even distribution of propellant between the remaining two spacecraft. The present study employs a preliminary Keplerian approximation for its cost evalua-

Table 9
ΔV breakdown for TASO capture scenario.

Man.	DV [km/s]	Gravity Losses	Margin Policy	DV [km/s]
First	0.940	10%	5%	1.087
Second	0.219	0%	5%	0.230
Third	0.408	10%	5%	0.472
TOT.	**1.567**			**1.789**

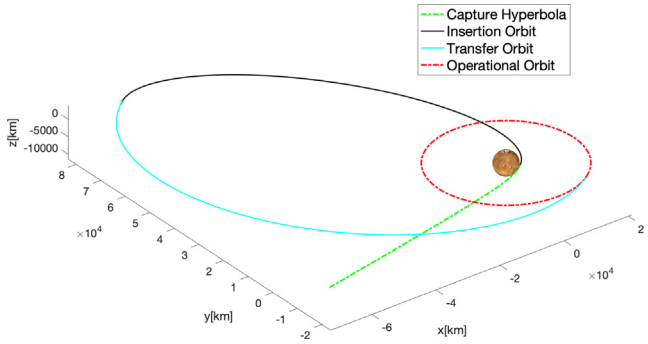

Fig. 14. TASO capture trajectory.

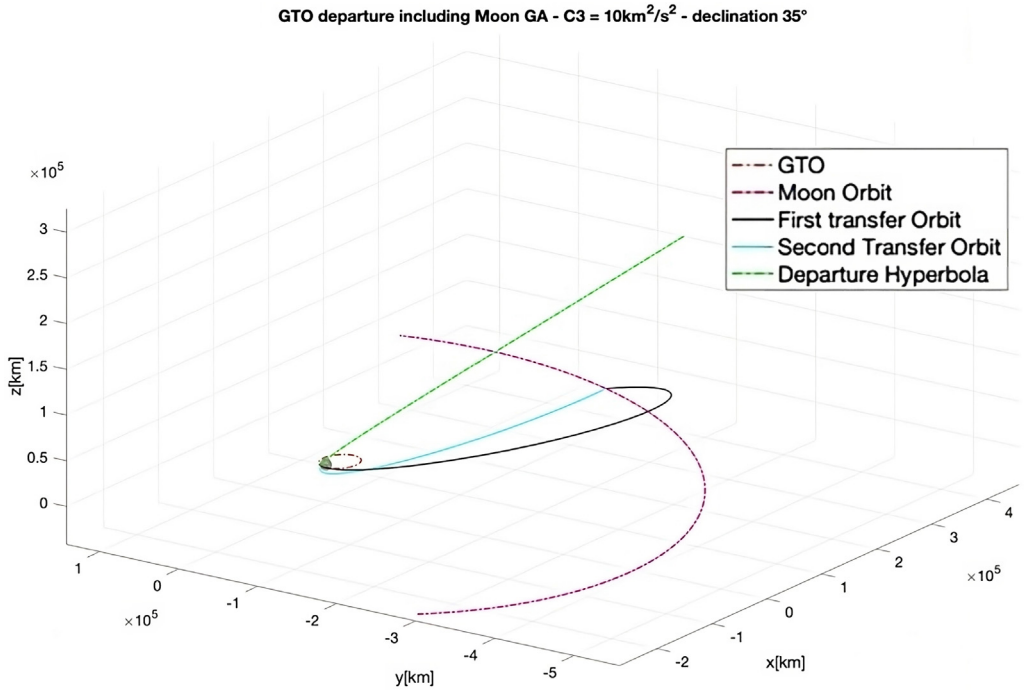

Fig. 13. GTO + Moon Gravity Assist escape ΔV map - constrained Local Time of Pericenter.

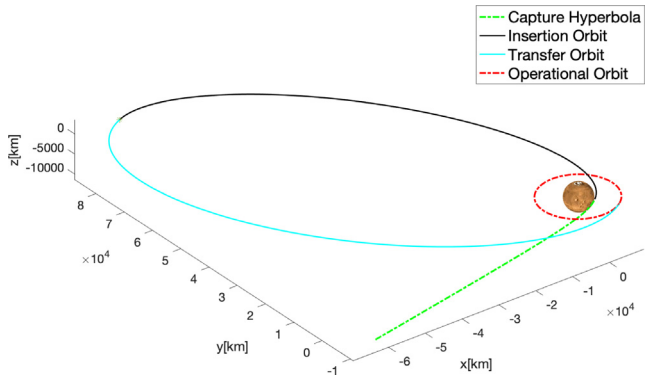

Fig. 15. Capture in Phobos Environment.

Table 10
ΔV breakdown for capture in Phobos environment.

Man.	DV [km/s]	Gravity Losses	Margin Policy	DV [km/s]
First	0.940	10%	5%	1.087
Second	0.099	0%	10 m/s	0.109
Third	0.751	10%	5%	0.867
TOT.	**1.79**			**2.063**

tion. Assuming the initial point to be on a perfectly circular orbit (with radius equal to the TASO, to Phobos' orbit, or to Deimos' orbit depending on the constellation), an impulsive manoeuvre is foreseen to change the energy of the orbit and introduce some drift. A second impulsive manoeuvre will inject the spacecraft back to the initial circular orbit on the desired location. The cost of such manoeuvres is a function the desired drift and the time available. The designed constellations require the spacecraft to be at 120° apart, so the only free variable is the drift time. Fig. 17 depicts the phasing costs for a single spacecraft as

Table 11
ΔV breakdown for capture in Deimos environment.

Man.	DV [km/s]	Gravity Losses	Margin Policy	DV [km/s]
First	0.940	10%	5%	1.087
Second	0.236	0%	5%	0.248
Third	0.367	10%	5%	0.424
TOT.	**1.543**			**1.759**

Table 12
TASO scenario transfer cost summary.

Phase	ΔV [km/s]				
	GTO	GTO constr	+ GA	HEO	Direct
Dep.	*1592*	*2074*	*1714*	*0781*	*0030*
Cap.			1780		
Tot.	**3372**	**3854**	**3494**	**2561**	**1810**

Table 13
Phobos scenario transfer cost summary.

Phase	ΔV [km/s]				
	GTO	GTO constr	+ GA	HEO	Direct
Dep.	*1592*	*2074*	*1714*	*0781*	*0030*
Cap.			2063		
Tot.	**3655**	**4.137**	**3.777**	**2.844**	**2093**

Table 14
Deimos scenario transfer cost summary.

Phase	ΔV [km/s]				
	GTO	GTO constr	+ GA	HEO	Direct
Dep.	*1592*	*2074*	*1714*	*0781*	*0030*
Cap.			1,759		
Tot.	**3351**	**3833**	**3473**	**254**	**1789**

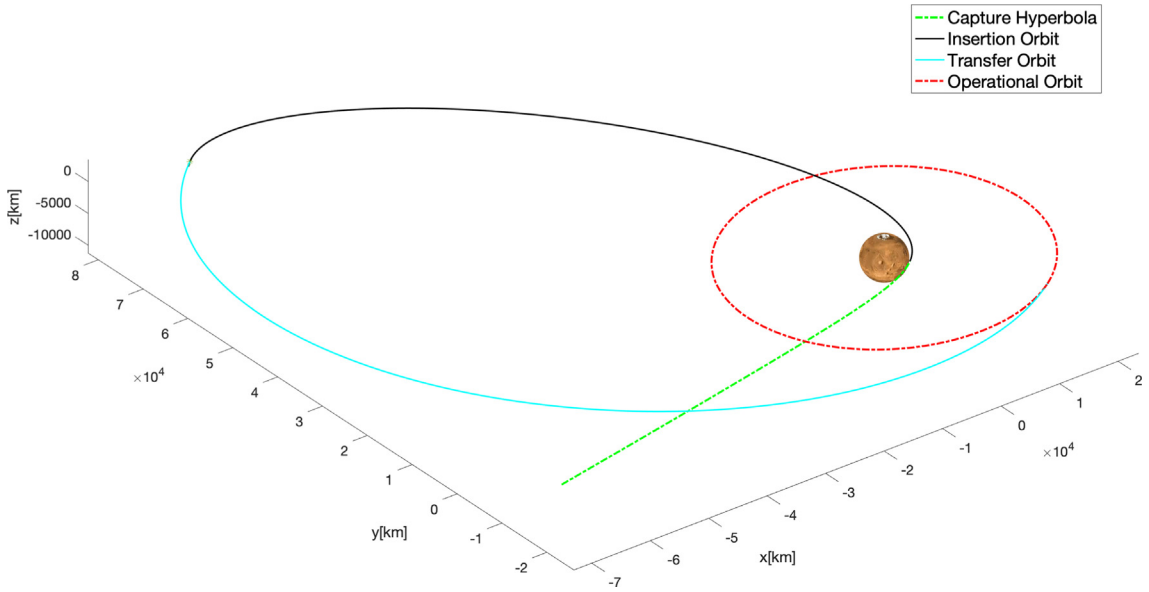

Fig. 16. Capture in Deimos Environment.

function of drifting time for the three orbital regimes of TASO, Phobos, and Deimos.

It can be noticed how the costs increase coherently with the altitude (at a fixed time of flight), due to the longer path needed to drift. In this regard, the Phobos constellation outperforms the others, with costs always lower than $15\,\mathrm{ms}^{-1}$ in the analysed time range. To balance the initialisation times and the costs, a drift of 30 days is here imposed, leading to a cost of $5\,\mathrm{ms}^{-1}, 11.2\,\mathrm{ms}^{-1}$ and $12.6\,\mathrm{ms}^{-1}$ for the Phobos, TASO, and Deimos constellations respectively.

Station-Keeping. In the TASO constellation case, it was previously shown that the no-drift condition can be attained by leveraging the irregular gravity of the red planet. It is therefore safe to state that, given the very small gravitational effect of Martian moons and the other planets in the TASO region, this constellation would be virtually free of station-keeping costs. Concerning the QSO + HS constellations, few considerations are required about relative drifts. Despite the good stability properties that both QSO and HS demonstrated in high-fidelity dynamics, the latter family is naturally characterised by secular drift that would disrupt the constellation geometry over time. It is then necessary to introduce periodic manoeuvres that force the spacecraft within a specific region of the natural trajectory by altering the natural drift direction (acting as phasing manoeuvres). A preliminary estimation of the costs of such "drift" control are provided for the nominal HS orbit in the CR3BP. Each spacecraft on the HS shall be located at a phase angle (i.e. the angle formed by the HS spacecraft and the moon, having Mars as vertex) about 120° from the moon. An angular drift threshold that triggers the station-keeping manoeuvre is then set. When the threshold is exceeded, a bi-impulsive transfer is optimised to "jump" from the outer side to the inner side of the HS orbit (or vice versa), which have an opposite direction of motion. By sequentially jumping from one branch to the other, the spacecraft will hover around the nominal phase region, within the set threshold. The optimisation process aims at minimising the total ΔV of the two impulses required to reach the other branch of the HS orbit.

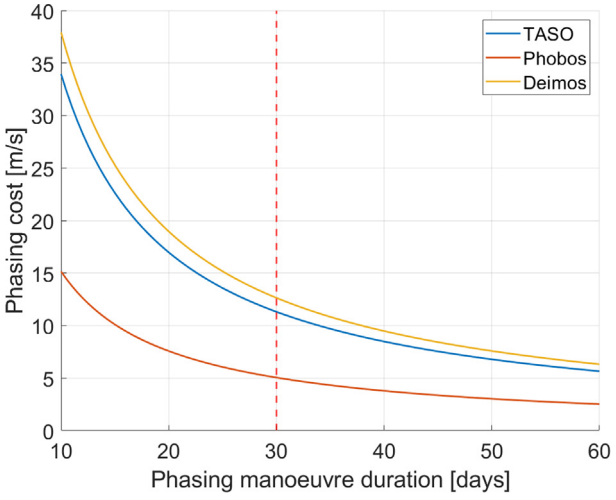

Fig. 17. Phasing cost for a single spacecraft as function of drifting time, for the three constellations analysed. The vertical red dashed line highlights the costs when a 30-days drifting is selected.

In the Phobos constellation scenario, the distance between the two orbit branches (in the CR3BP model) is around is 1 km, and the transfer requires $0.11\,\mathrm{ms}^{-1}$. Given the faster motion of satellites with respect to the Martian surface, drifts up to ±10° are acceptable, leading to approximately one manoeuvre every 4 months. Considering a mission duration of 6 years both spacecraft on the HS in the Phobos environment will require approximately $2\,\mathrm{ms}^{-1}$ for station-keeping. In the Deimos environment, instead, the orbital speed is comparable with Mars' rotation, hence a smaller drift of 2° is set. Given the larger distance between the forward and backward branches of the orbit (4.7 km), and the time of 12 days to reach the maximum deviation, a set of approximately 90 manoeuvres of $0.14\,\mathrm{ms}^{-1}$ each is needed, leading to $12.85\,\mathrm{ms}^{-1}$ per spacecraft on the HS.

Overall, margined costs (following ECSS guidelines (HRE-XE-ESA, 2017)) of phasing and station-keeping are reported in Table 15.

It is observed that the Deimos environment represents the worst option in terms of manoeuvre costs during the operative life. Also, the TASO configuration appears to be similar in cost to the Phobos configuration, but such cost may be subjected to significant increment if constellation initialisation errors are introduced.

4.4. Communication performances

In this section, the performances in terms of communication capabilities of the constellation are reported with respect to a test user located at the equator. The choice of the configuration among the ones presented in the paper does not significantly influence the Earth-link in terms of both datarate and visibility, given the fact that the Earth-Mars distance is much larger than the distance from the Mars' surface to the analysed orbits. Hence, only the satellite-to-ground link is considered as figure of merit for the configuration's definition.

To compute the data-rate, the link budget was evaluated dynamically along the satellites' trajectories. For the telecommunication hardware, Elektra-Lite communication protocols (Edwards, 2003) compatible parameters were taken into account, according to CCSDS standards. All

Table 15
Margined phasing and station-keeping costs for the proposed configurations.

Constellation	TASO	Phobos	Deimos
Phasing [m/s]	42.4	30	45.2
Station Keep. [m/s]	0	8	51.6
Total [m/s]	**42.4**	**38**	**96.8**

the data used for the performance evaluation is reported in Table 16.

In Table 17 the figures of merit for Deimos architecture are reported, compared to TASO results.

In this analysis, the user is located at the equator. t_W is the single communication window duration between the user and the satellite. t_V is the visibility time per day, which corresponds to the sum of the single user-satellite windows' duration. The visibility gap t_G is instead the amount of time between two consecutive visibility windows, in which communication doesn't take place. The interruption of communication can be caused by the insufficient E_b/N_0 to achieve data transmission or by the geometrical occultation when the satellite elevation angle is lower than the fixed threshold of 10°. For a satellite located in a QSO or HS orbit in the Mars-Deimos environment, the visibility window lasts up to $33h$. This is caused by the slow relative drift with respect to the surface since Deimos orbit's altitude is close to the TASO region. On the other hand, this causes a high gap of $9h$ between two consecutive visibility windows. Due to the altitude increase, the data-volume D is reduced with respect to TASO (204.12 Mb/day versus 259.2 Mb/day for TASO).

Analogously, Mars-Phobos architecture's figures of merit have been computed and are reported in Table 17. For Phobos configuration, the visibility window duration t_W is reduced to 4 h. Anyway, for Phobos the relative drift with respect to Mars's surface is higher, leading to the overlapping of two subsequent windows. Hence, continuous visibility can be achieved for this scenario. This visibility time and data-rate increase lead to a higher daily data-volume D with respect to TASO, up to 942 Mb/day.

For clarity, the data-rate behaviour over time for the Phobos configuration is reported in Fig. 18.

Note that the overlapping of the windows is dependent on the achieved data-rate and can lead to a reduced service when higher latitudes are considered. Indeed, the maximum data-rate achievable depending on the user latitude is reported in Fig. 19.

As expected, the maximum data-rate achievable corresponds to the equatorial region and it is higher for the Mars-Phobos architecture with respect to TASO satellites. It is also interesting to note that over 35° latitude the values reached are similar, while the Mars-Phobos architecture allows reaching higher latitudes (up to 76°) with respect to TASO satellites (65° maximum).

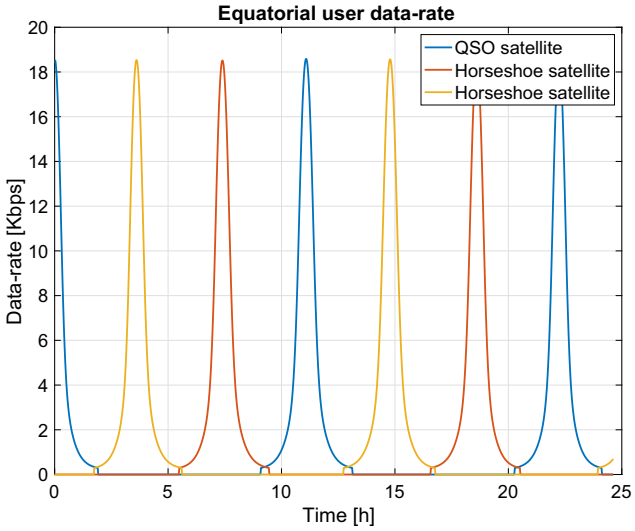

Fig. 18. Data-rate evolution for the Mars-Phobos architecture, considering an equatorial user.

Table 16
Link budget hardware parameters.

Parameter	Unit	Value
Frequency	MHz	400
Tx Power	W	4
Tx Antenna Gain	dBi	−3.15
Tx Losses	dB	1
Atmosphere Losses	dB	5
Rx Polarization Losses	dB	0.8
Rx G/T	dBK	−25.23
Demodulation Losses	dB	1
Modulation Losses	dB	0
Minimum E_b/N_0 margin	dB	3

Table 17
Deimos architectures performances compared to TASO.

Architecture	t_W	t_V	t_G	D
TASO	24 h	24 h	0 h	259.2 Mb/day
Deimos	33 h	33 h	9 h	204.12 Mb/day
Phobos	4 h	24 h	0 h	942 Mb/day

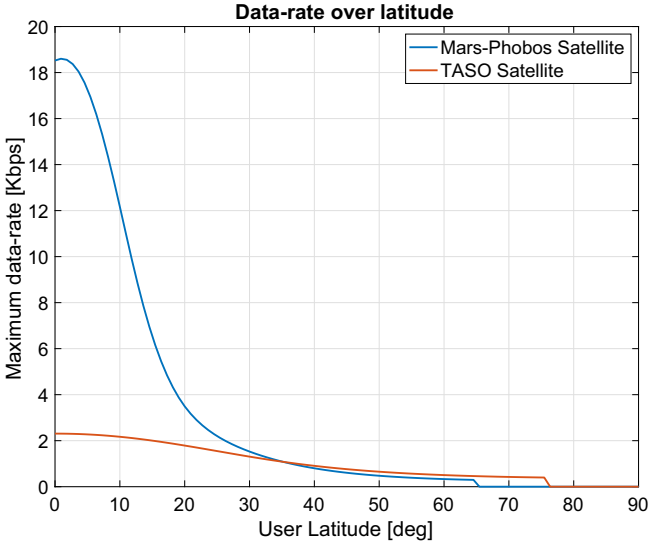

Fig. 19. Maximum data-rate of the satellite-user link depending on the user latitude, for both Phobos and TASO configurations.

5. Autonomous navigation

Since the satellites in the multi-body regimes constellations follow non-keplerian trajectories, the asymmetry of the field allows reconstructing their absolute states with relative measures only (Hill, 2007). For autonomous state calibration to be possible, at least one of the trajectories involved shall have an out-of-plane component different from zero. This can be achieved by exploiting inclined QSOs, leading to full observability of the system composed of the three satellites.

In this analysis, a set of QSOs ranging from $0km$ to $8.34km$ out-of-plane component $\hat{z}$ has been selected. The trajectories are shown in Fig. 20, while the related observability index variation is reported in Fig. 21. The observability index has been computed as the conditioning number of the Gramian matrix representing the variation of the state with respect to the relative measure (Kaufman et al., 2016).

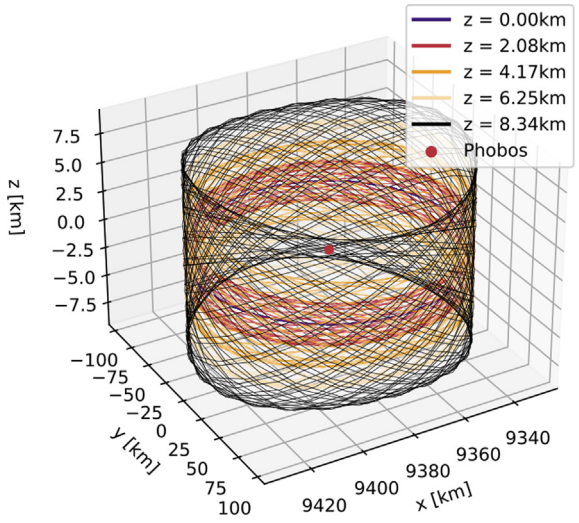

Fig. 20. Inclined QSO trajectories in the Mars-Phobos system.

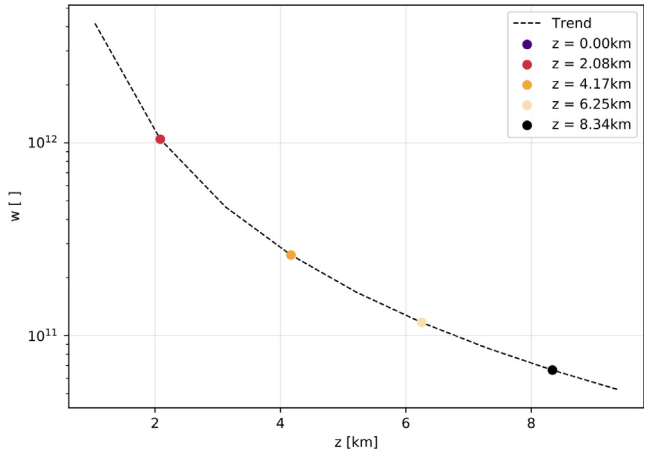

Fig. 21. System conditioning number with respect to QSO out-of-plane component for the analysed configurations.

As can be seen, the system is numerically observable, since the conditioning number w is lower than 10^{16}, and the observability increases (the conditioning number decreases) as the out-of-plane component increases. Note that the case in which all the trajectories are planar is not reported since the observability index would increase up to infinity.

The case in which the $\hat{z}$-component is the maximum considered and equal to $8.24km$, is taken as a reference scenario to simulate the self-calibration algorithm. The state reconstruction is performed through a Square Root - Unscented Kalman Filter (SR-UKF) (Van Der Merwe and Wan, 2001; Barberi Spirito, 2021). Indeed, when dealing with a

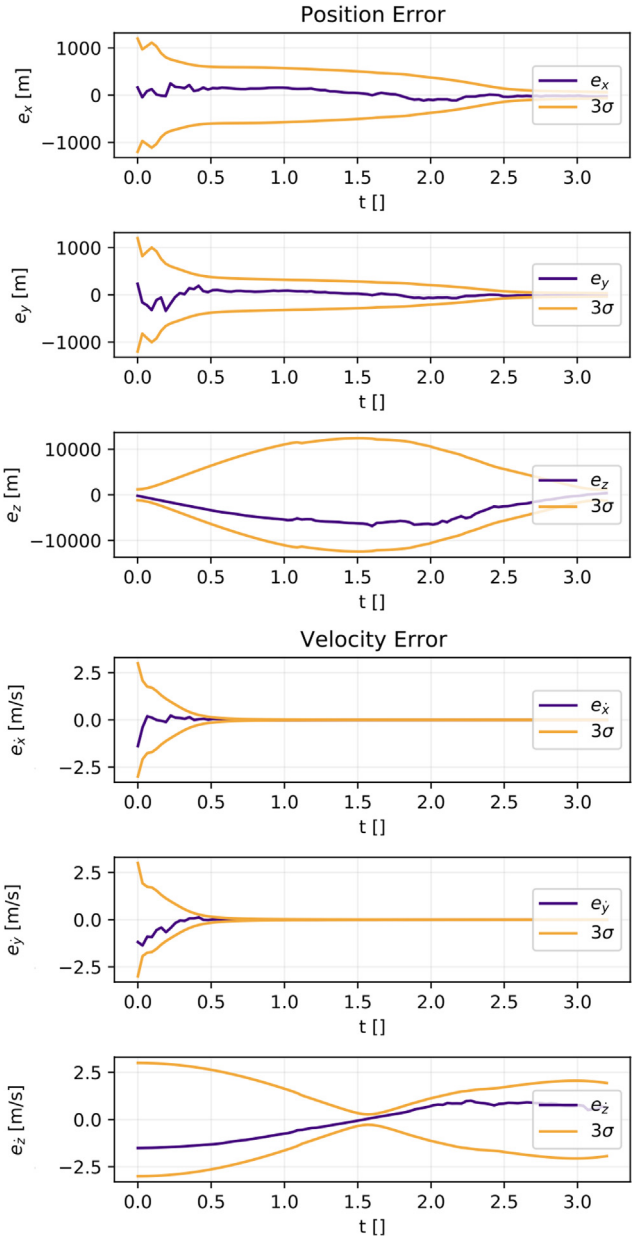

Fig. 22. HS satellite state error and standard deviation over time during SR-UKF reconstruction. e represents the error with respect to the single component of the state.

highly non-linear problem, if the initial estimate is not accurate enough, the state error covariance matrix can lose its property of semi-positive definiteness, leading to the divergence of the filtering scheme. A Square-Root algorithm can mitigate this problem by exploiting a Cholesky decomposition of the covariance matrix, forcing its positive-definiteness during the propagation. 100 range and range-rate measurements were simulated and fed into the filter in a period of 3.2 non-dimensional time units, corresponding to almost 3.5 h. This corresponds to a measurement sample acquired every 139s.

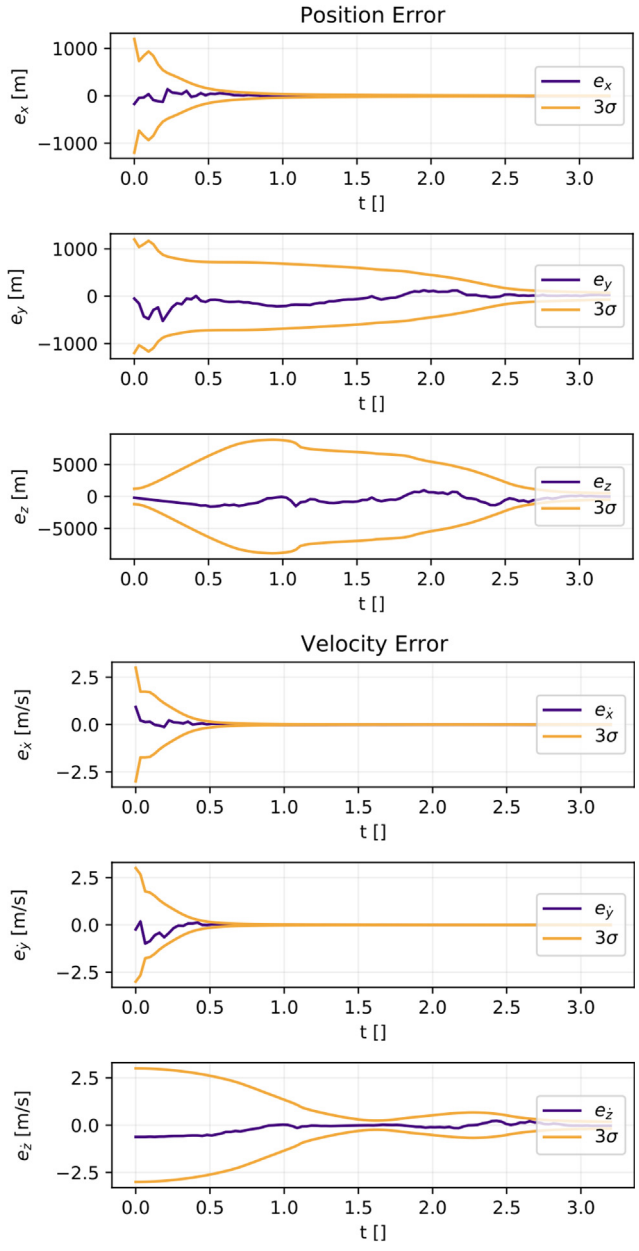

Fig. 23. QSO satellite state error and standard deviation over time during SR-UKF reconstruction. e represents the error with respect to the single component of the state.

For the method to succeed, the a priori knowledge of the out-of-plane component shall have an uncertainty lower than the value of the $\hat{z}$-component itself (Hill, 2007). Hence, the initial standard deviation considered for the simulation is $\sigma_p = 400m$ for position and $\sigma_v = 3m/s$ for velocity. Results are reported in Fig. 22 for the satellite in HS and Fig. 23 for the one in QSO, where the error of the recostruction for all the components of the state are shown.

The reconstructed state converges to the real one for all the components except for the z component of the HS satellite. The final three-sigma accuracy is $63m$ for position and $1mm/s$ for velocity. The out-of-plane component of the QSO satellite converges too, but with a higher final error of $801m$ for the position and $0.12m/s$ for velocity.

6. Conclusion

As reported in Section 4.4, the visibility windows for a single satellite of the Phobos constellation are shorter with respect to TASO and longer for Deimos satellites. Anyway, the Deimos constellation presents a drastic increase in the non-visibility gap (9 h), while at least one satellite of the Phobos constellation is always visible at the equator. Hence, higher data-volume is obtained by Phobos architectures (942 Mb versus 259.2 Mb of TASO) and lower for Deimos (204.12 Mb).

Depending on the mission constraints (cost, required data-volume and visibility) Phobos and TASO architectures are both suitable options for a communication constellation, while Deimos architectures showed to be inconvenient since such a constellation would drastically reduce the visibility with a low gain on propellant mass.

Moreover, a Phobos architecture has proved to be observable and capable to reconstruct the absolute state of the satellites with range and range rate measurements only, if the QSO satellite is initialised with a non-zero out-of-plane component. This can be a good starting point for the definition of an autonomous navigation strategy that can enlighten the requirements in terms of direct-Earth tracking of the constellation satellites.

In Section 4.2 the possible transfer strategies between Earth and the operative orbits of the three configurations were discussed in detail.

While the direct option is less demanding in terms of propellant mass, it can be more expensive to have a dedicated launch for the mission. The other strategies increase the amount of propellant needed for the interplanetary trajectory insertion manoeuvre, but the selection of the launch can be more flexible: a piggyback solution to another mission can be less expensive, taking into account that the platform shall be bigger to host extra propellant for the additional manoeuvre. For what concerns the Mars Capture, as expected Phobos orbit is more expensive to reach due to its lower altitude, while Deimos needs the lower ΔV budget. Regarding the phasing and station-keeping

ΔV, there is no significant variation between Phobos and TASO architectures.

References

Andrews, D.H., 1930. The theory of the potential (macmillan, william duncan). J. Chem. Educ. 7 (10), 2530. https://doi.org/10.1021/ed007p2530, arXiv:https://doi.org/10.1021/ed007p2530.

Arianespace 2021. Ariane 6 User Manual - Issue 2. Ariane Group.

Barberi Spirito, D., 2021. Martian assets navigation service through Mars-Phobos multi-body regime exploitation for constellation design. M.Sc. Thesis at Politecnico di Milano.

Barberi Spirito, D., Capannolo, A., Prinetto, J., et al., 2021. Mars-phobos system dynamics exploitation for martian effective constellations design. In 72nd International Astronautical Congress (IAC 2021) (pp. 1–9).

Battin, R.H., 1999. An introduction to the mathematics and methods of astrodynamics. AIAA, Reston, VA.

Bell, D., Allen, S., Chamberlain, N., et al., 2014. MRO relay telecom upport of Mars science laboratory surface operations. In: In 2014 IEEE Aerospace Conference. IEEE, pp. 1–10.

Belousov, S.L., 2014. Tables of Normalized Associated Legendre Polynomials: Mathematical Tables Series. Elsevier.

Castellini, F., Simonetto, A., Martini, R., et al., 2010. A mars communication constellation for human exploration and network science. Adv. Space Res. 45, 183–199. https://doi.org/10.1016/j.asr.2009.10.019.

Conway, B.A., Paris, S.W., 2010. Spacecraft trajectory optimization using direct transcription and nonlinear programming. In: Conway, B.A. (Ed.), Spacecraft Trajectory Optimization Cambridge Aerospace Series. Cambridge University Press, pp. 37–78. https://doi.org/10.1017/CBO9780511778025.004.

Edwards, C.D. (2003). The electra proximity link payload for mars relay telecommunications and navigation. In 54th International Astronautical Congress of the International Astronautical Federation, the International Academy of Astronautics, and the International Institute of Space Law (pp. Q–3).

Edwards, C.D., Barela, P.R., Gladden, R.E., et al., 2014. Replenishing the mars relay network. In: In 2014 IEEE Aerospace Conference. IEEE, pp. 1–13.

Hill, K.A., 2007. Autonomous navigation in libration point orbits. University of Colorado at Boulder, Ph.D. thesis.

HRE-XE-ESA (2017). Margin Philosophy for Mars Exploration Studies, ESA-E3P-MSR-RS-001. European Space Agency.

Isoletta, G., Grassi, M., Fantino, E., et al., 2021. Feasibility study of aerocapture at mars with an innovative deployable heat shield. Journal of Spacecraft and Rockets 58 (6), 1752–1761.

Kaufman, E., Lovell, T.A., Lee, T., 2016. Nonlinear observability for relative orbit determination with angles-only measurements. The Journal of the Astronautical Sciences 63 (1), 60–80. https://doi.org/10.1007/s40295-015-0082-9.

Kennedy, J., & Eberhart, R. (1995). Particle swarm optimization. In Proceedings of ICNN'95 - International Conference on Neural Networks (pp. 1942–1948 vol 4). volume 4. doi:10.1109/ICNN.1995.488968.

Montabone, L., Heavens, N., Alvarellos, J.L., et al., 2020. Observing Mars from areostationary orbit: Benefits and applications. Planetary Science and Astrobiology Decadal Survey, 2023–2032.

Parfitt, C.E., McSweeney, A.G., De Backer, L., et al., 2021. Small mars mission architecture study. Advances in Astronomy 2021, 5516892. https://doi.org/10.1155/2021/5516892.

Pearl, J., 1984. Heuristics: intelligent search strategies for computer problem solving. Addison-Wesley Longman Publishing Co. Inc., Boston, US.

Penzo, P.A. (1998). Planetary missions from gto using earth and moon gravity assists. In AIAA Astrodynamics Specialist Conference.

Poli, R., 2008. Analysis of the publications on the applications of particle swarm optimisation. J. Artif. Evol. Appl. 2008. https://doi.org/10.1155/2008/685175.

Prinetto, J., Lavagna, M., 2021. Elliptical shape-based model for multi-revolution planeto-centric mission scenarios. Celestial Mech. Dynam. Astron. 133 (1), 1–24. https://doi.org/10.1007/s10569-020-10001-9.

Topputo, F., Zhang, C., 2014. Survey of direct transcription for low-thrust space trajectory optimization with applications. In Abstract and Applied Analysis. Hindawi 2014. https://doi.org/10.1155/2014/851720.

Van Der Merwe, R., Wan, E.A., 2001. The square-root unscented kalman filter for state and parameter-estimation. In: 2001 IEEE International Conference on Acoustics, Speech, and Signal Processing. Proceedings (Cat. No. 01CH37221) (pp. 3461–3464). IEEE volume 6. doi:10.1109/ICASSP.2001.940586.